Designing oxidation resistant ultra-high temperature ceramics through the development of an adherent native thermal barrier

Gaoyuan Ouyang [a, b, *], Matthew F. Besser [b], Matthew J. Kramer [a, b], Mufit Akinc [a, b], Pratik K. Ray [a, b]

[a] Department of Materials Science and Engineering, Iowa State University, Ames, IA, 50011, USA
[b] Ames Laboratory, US-DOE, Ames, IA, 50011, USA

ARTICLE INFO

ABSTRACT

We present a design concept for developing ZrB_2-SiC-AlN composites with enhanced oxidative stability at ultra-high temperatures (~2000 °C) and low pressures (100 Torr). The oxidative stability of these materials arises from a protective silica based scale. However, active oxidation of SiC above 1700 °C presents a challenge, which we circumvent through the in-situ growth of a zirconia layer that serves as a thermal barrier, ensuring that the effective temperature at the zirconia/Si rich subscale is less than the active oxidation temperature. The design concept is validated by a series of ultra-high temperature oxidation experiments under static as well as cyclic conditions.

© 2019 Elsevier B.V. All rights reserved.

1. Introduction

Thermal protection systems in hypersonic vehicles call for a unique combination of properties required for meeting the challenges of harsh environments. At extreme velocities (mach 7 or higher), the temperatures at the leading edges of hypersonic aircrafts can often exceed 1800 °C as a result of aerodynamic heating during the re-entry phase. At stratospheric conditions, the oxygen pressures are extremely low, and such high enthalpy conditions results in the dissociation, forming air plasma. Such conditions require that the material system be (1) resistant to high temperatures; (2) have a high thermal conductivity for conducting away the heat and (3) have adequate oxidation resistance under static and cyclic conditions, with the latter being especially critical for reusability of the thermal protection system. Recent efforts have identified ZrB_2-SiC system to be a potentially viable candidate system for these applications, especially in light of their high melting temperatures, and formation of a silica scale [1—4]. Nonetheless, as the temperature exceeds 1700 °C, active oxidation of SiC prevents the formation of a protective scale [5—7].

In this paper, we propose a design concept for future development of ZrB_2-SiC composites, similar to Ni-based superalloys. The operational temperatures of Ni-based superalloys are limited by the formation of low melting topologically close-packed phases, as well as a loss of creep resistance above 900 °C. As these alloys approach their limits, the range of operational temperatures is expanded via active cooling and thermal barrier coatings. We recognize that the ZrB_2-SiC composites have the potential for an *in-situ* natively grown thermal barrier, in the form of zirconia. Underneath this "native" thermal barrier, the presence of a silica rich scale will provide the oxidation resistance. Zirconia, however, has relatively poor thermal shock resistance. Failure of the zirconia through thermal shock, especially under cyclic conditions, is therefore identified as a key factor that limits the reusability of the material system. Our concept is based around mitigating the shock by ensuring the presence of a subscale pliable enough to accommodate the thermal expansion and contraction of the overlying zirconia, yet tenacious enough to retain the zirconia grains. This is achieved by appropriately adjusting the viscosity of the underlying subscale, and builds on our previous work where we demonstrated addition of AlN can result in significant modifications of the viscosity [8,9]. Past efforts have indicated that addition of AlN results in improved densification of ZrB_2-SiC composites under hot pressing conditions. Additionally, AlN is a high melting ceramic that has excellent thermal conductivity — which is certainly desirable in a thermal protection system.

In the present work, we investigate the oxidation behavior of a number of ZrB_2-SiC-AlN composites at temperatures higher than 1900 °C at a pressure of 100 Torr under cyclic and static conditions

---

* Corresponding author. Department of Materials Science and Engineering, Iowa State University, Ames, IA, 50011, USA.

E-mail address: gaoyuan@iastate.edu (G. Ouyang).

in order to showcase our design concept. The experimental results corroborate our proposition, with the ultra-high temperature oxidation resulting in the formation of a multilayered scale comprising of an external ZrO_2 layer and a silica rich subscale. The stability of subscale, especially under cyclic conditions, indicate that the active oxidation has been arrested, which lends credence to our hypothesis that the primary role of the polycrystalline ZrO_2 in the oxidation of these materials is to provide a thermal barrier layer leading to a drop in the temperature at the internal ZrO_2/ subscale interface.

2. Experimental details

Commercially-available powders were used as raw materials: ZrB_2 (Grade B, ~2 μm particle size, H.C.Starck, Karlsruhe, Germany) SiC (Grade UF-10, ~1 μm particle size, H.C.Starck, Karlsruhe, Germany), and AlN (Grade C, ~1 μm particle size, H.C.Starck, Karlsruhe, Germany). Nominal compositions of ZrB_2-30 vol%SiC (ZS73), ZrB_2-30 vol%SiC-10 vol%AlN (ZSA631), ZrB_2-20 vol%SiC (ZS82), ZrB_2-20 vol%SiC-10 vol%AlN (ZSA721) were prepared and studied in this paper. Samples were prepared using a method described in our previous paper [8], in accordance with the approach adopted from Zhang et al. [10]. Powders were mixed and milled in plastic jars with methyl ethyl ketone using tungsten carbide as milling media. Organic binder (QPAC40, polypropylene carbonate, Empower Materials Inc., New Castle, DE) was added in the milling procedure to increase the density of the green body. Binder-coated powders were harvested from the mixture using roto-evaporation followed by grinding and sieving through 44 μm screen. Cylindrical compacts with a diameter of ~12 mm and height of ~20 mm were uniaxially pressed followed by cold isostatic pressing at 310 MPa. Binder removal was completed at 600 °C in flowing argon atmosphere prior to the sintering. A sintering temperature of 2000 °C was used for 30 vol% SiC samples, while 2200 °C was used for 20 vol % SiC samples. Both sintering profiles included two 1-h isothermal holds at 1250 and 1450 °C in vacuum to remove the surface oxides. The sintering was done in a resistively heated furnace with graphite heating elements (3060-FP20, Thermal Technology Inc., Santa Rosa, CA). The sintered densities were measured according to ASTM standard B962-15 [11] using Archimedes principle. Relative density was expressed as a fraction of calculated theoretical density for each composition.

A plasma gun (SG-100, Praxair Surface Technologies, Indianapolis, IN), with a power input of 40 kW was used for heating the test samples to the target temperature (2000 °C). Argon (flow rate: 80 SCFH (standard cubic feet per hour)) was used as the plasma gas and helium (flow rate: 44 SCFH) was used as the auxiliary gas. A ZrO_2 coated graphite tube with a hollow push rod was utilized to hold the test specimen. A separate vacuum line was used against the rear surface of the sample through the push rod to hold the sample in place. A manual sliding sample holder system was designed to change the sample standoff (distance from the sample's anterior surface to the plasma gun). The gun and sample holder were placed inside a vacuum chamber. A pressure of 100 Torr was used for the test with continuous air supply. The oxygen content was measured as 21% by an oxygen sensor (MAX-250E, Maxtec Inc, Murray, UT), whose probe was placed ~1 inch from the sample front surface. Sample surface temperature was measured by a two-color optical pyrometer (Modline 5R-3015, Ircon Inc., Santa Cruz, CA). The pyrometer was calibrated using type R/S thermal couple (Omega Engineering Inc., Stamford, CT) and black body with the accuracy of the measurements as ± 10 °C. The layout of the experimental setup is shown in Supplemental Information Fig. S1.

All compositions were subjected to 10-min one and five-cycles testing. The sample was place 6 mm above the holder (with

~14 mm inside the hollow holder) for each test. The front surface and the 6 mm length side surface were included in the surface area calculation. All tests started at an identical standoff to maintain an identical initial heating rate. The standoff was adjusted manually during the test to maintain 2000 (±50)°C for 10 min. For the cyclic tests, the samples were cooled in a vacuum for 30 min with the plasma gun off before it was removed for measurement and inspection, and then reloaded for the next cycle. The temperature was recorded during testing via ModView software (Ircon Inc., Santa Cruz, CA) at 1.5 s intervals. The temperature profile for ZS73 cyclic testing is shown in Supplemental Information Fig. S2. All other tests maintained similar temperature profiles. The sample mass was measured after each cycle. The sample surface was analyzed by SEM (Quanta-250, FEI Company, Hillsboro, Oregon) and XRD (Philips PANalytical, Almelo, The Netherlands), the cross-section was examined by stereo microscope (SZX12, Olympus Co., Tokyo, Japan) with a digital camera (DP21, Olympus Co., Tokyo, Japan), SEM and EDS (Oxford Aztec, Oxford Instruments, Abingdon, United Kingdom). The XRD patterns were obtained using Cu Kα radiation in Bragg-Brentano reflection geometry.

3. Volatility diagram

To understand the thermal stability of each phase, a volatility diagram was constructed. The chemical reactions involved are tabulated in Table 1 where chemical reactions for boron and silicon were cited from the literature [4,5]. Thermodynamics data and equilibrium constants were extracted from the NIST-JANAF tables [12]. The volatility diagram in Fig. 1a covers the species with the highest vapor pressure at each oxygen partial pressure P_{O2}.

As shown in the volatility diagram, the significant vapor species in this system are B_2O_3, SiO, and Al_2O. Therefore, a separate graph of vapor pressure containing these species as a function of temperature is calculated and plotted in Fig. 1b. B_2O_2 is also considered, since it has comparable vapor pressure to B_2O_3 at the ZrB_2-ZrO_2 interface and has a higher vapor pressure than B_2O_3 at the lower oxygen partial pressure regime. ZrO is the most dominant vapor specie among the Zr species, so it is also plotted on the diagram. SiO_2 is also considered, due to its high vapor pressure at high oxygen partial pressures. Vapor pressures of B_2O_3 and SiO_2 are in equilibrium with their corresponding liquid and independent of P_{O2}. Since SiO has the highest vapor pressure at Si-SiO_2 interface [13], P_{O2} at this interface was utilized. A similar approach was used for ZrO, Al_2O, and B_2O_2 to determine the P_{O2} needed. The calculated vapor pressures are in good agreement with the work of Opeka et al. [13].

The volatility diagram suggests that a silica based scale would be unstable at the gas/solid interface, due to the loss of Si as SiO. Similarly, the vapor pressure of B_2O_3, as well as prior research on the volatilization of B_2O_3 implies that B_2O_3 cannot remain at the gas/solid interface [14]. Therefore, the only possible oxides that can be stable in the external scale is Al_2O_3 and ZrO_2. However, ZrO_2 has an extremely low thermal conductivity, as a result of which the subscale temperatures would be substantially lower leading to the presence of a silica rich scale deeper in the composite. This has in fact been observed by a number of researchers. Hence, the volatility diagram suggests that the oxidation resistance of this material can be improved if the ZrO_2 layer in the oxide scale can be preserved. While, under isothermal conditions, this would not be problematic, cyclic conditions would induce thermal shocks. A thermal shock damage mitigation mechanism is therefore essential to prevent ZrO_2 layers from spalling off, which is our focus in the remainder of the paper.

Table 1
Reactions used in ZrB$_2$-SiC-AlN system.

| Reactions with ZrB$_2$ as condensed phase	Reactions with B$_2$O$_3$ as condensed phase
ZrB$_2$ (cr) +3O$_2$ (g) → ZrO$_2$ (cr)+2BO$_2$ (g)	B$_2$O$_3$(l) → B$_2$O$_3$(g)
ZrB$_2$ (cr) + 2.5O$_2$ (g) → ZrO$_2$ (cr)+ B$_2$O$_3$ (g)	B$_2$O$_3$(l) + 0.5 O$_2$(g) → 2BO$_2$(g)
ZrB$_2$ (cr)+2O$_2$ (g) → ZrO$_2$ (cr)+B$_2$O$_2$ (g)	B$_2$O$_3$(l) → B$_2$O$_2$ (g) + 0.5O$_2$ (g)
ZrB$_2$ (cr)+2O$_2$ (g) → ZrO$_2$ (cr)+2BO (g)	B$_2$O$_3$(l) → 2BO(g) + 0.5O$_2$ (g)
ZrB$_2$ (cr) + 1.5O$_2$ (g) → ZrO$_2$ (cr)+B$_2$O (g)	B$_2$O$_3$ (l) → B$_2$O (g) + O$_2$ (g)
ZrB$_2$ (cr)+O$_2$ (g) → ZrO$_2$ (cr)+B$_2$ (g)	B$_2$O$_3$ (l) → B$_2$ (g) + 1.5O$_2$ (g)
ZrB$_2$ (cr)+O$_2$ (g) → ZrO$_2$ (cr)+2B (g)	B$_2$O$_3$ (l) → 2B (g) + 1.5 O$_2$ (g)
Reactions with SiC as condensed phase	Reactions with SiO$_2$ as condensed phase
SiC (cr) + 1.5O$_2$ (g) → SiO$_2$ (g) + CO (g)	SiO$_2$ (l) → SiO$_2$ (g)
SiC (cr) + O$_2$ (g) → SiO (g) + CO (g)	SiO$_2$ (l) → SiO (g)+ 0.5O$_2$ (g)
SiC (cr) + 0.5O$_2$ (g) → Si (g) + CO (g)	SiO$_2$ (l) → Si (g)+ O$_2$ (g)
Reaction with AlN as condensed phase	Reaction with Al$_2$O$_3$ as condensed phase
AlN (cr) +O$_2$ (g) →AlO (g) + NO (g)	Al$_2$O$_3$ (cr) → 2AlO (g) + 0.5O$_2$ (g)
AlN (cr) +1.5O$_2$ (g) →AlO$_2$ (g) + NO (g)	Al$_2$O$_3$ (cr) +0.5 O$_2$ (g) → 2AlO$_2$ (g)
AlN (cr) +0.5O$_2$ (g) →0.5Al$_2$ (g) + NO (g)	Al$_2$O$_3$ (cr) → Al$_2$ (g) + 1.5O$_2$ (g)
AlN (cr) +0.75O$_2$ (g) →0.5Al$_2$O (g) + NO (g)	Al$_2$O$_3$ (cr) → Al$_2$O (g) + O$_2$ (g)
AlN (cr) +O$_2$ (g) →0.5Al$_2$O$_2$ (g) + NO (g)	Al$_2$O$_3$ (cr) → Al$_2$O$_2$ (g) + 0.5O$_2$ (g)
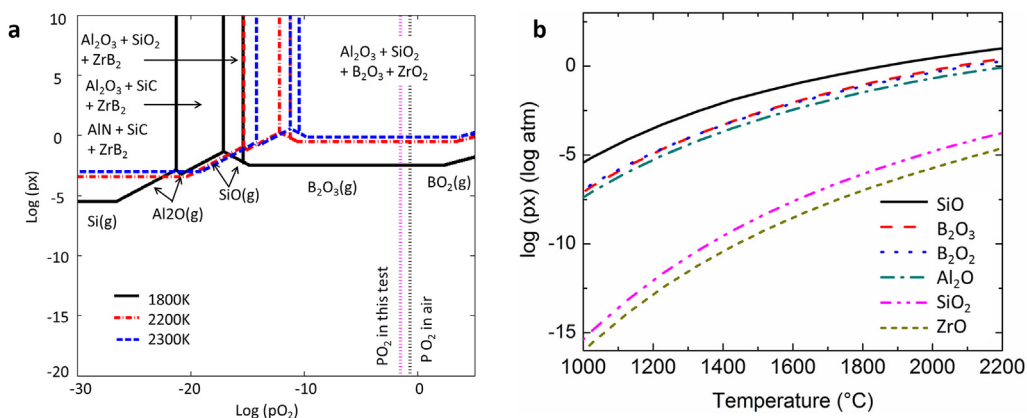
Fig. 1. a. ZrB$_2$-SiC-AlN volatility diagram; b. Vapor pressure of relevant vapor species as a function of temperature.

4. Results and discussion

All samples achieved a relative density of 93% or higher. Fig. 2 shows the microstructures of the sintered samples. SiC or a combination SiC and AlN (dark phase) was well distributed in the ZrB$_2$ matrix (bright phase). It has been reported in the literature that addition of SiC results in improved densification of ZrB$_2$-SiC composites [15]. Consequently, a higher sintering temperature (2200 °C as opposed to 2000 °C for the ZS73 and ZSA631) was required for samples with lower SiC content (ZS82 and ZSA721) in order to attain significant densification. Higher sintering temperature possibly accounts for a coarser grain structure of ZS82 and ZSA721 in comparison to ZS73 and ZSA631. Since AlN and SiC have very similar Z contrast, it is not possible to distinguish these two phases with backscattered electron imaging. Both of the two phases appeared dark in the backscattered images. Fig. 2(e) and (f) show the elemental Al distribution acquired using EDS. Comparing EDS maps in 2(e) and (f) between 2(b) and (c), Al is present in only a portion of the dark contrast phase features. The remaining of the dark phase has high Si content. AlN and SiC phases are thus believed present in separate phases. The difference in size of the AlN features also form the same trend as ZrB$_2$ phases.

Oxidation at ~2000 °C for 10 min resulted in the development of a yellowish oxide layer. XRD patterns from the sample surface showed the formation of a ZrO$_2$ layer, with small amounts of SiO$_2$ (crystoballite) as seen in Fig. 3. Fig. 4 shows the SEM images of the

surface after a 10-min oxidation at 2000 °C. The bright phase represents ZrO$_2$. The SEM observations are consistent with the XRD patterns of the surface, as only ZrO$_2$ (confirmed by EDS) is seen on the ZS73 sample surface, while ZrO$_2$ coexists with a darker phase in other compositions. Most the surface structures of ZS73 were comprised of discrete clusters of ZrO$_2$. Large channels (or pores) were present in between the ZrO$_2$ clusters. ZSA631 shows a completely different microstructure compared to the other three samples, with the surface showing a fine lamellar morphology. EDS analyses indicated the presence of Al, Si, and oxygen in the surface scale. Most the ZS82 surface reveals ZrO$_2$ agglomerates and the Si-O rich phase as shown in Fig. 4c. ZSA721 shows similar microstructures as compared to ZS82 with a ZrO$_2$ (bright phase) and regions rich in Al, Si, and O (dark phase). The porous ZrO$_2$ scale formed in ZS73 (Fig. 4a) cannot be expected to provide adequate oxidation resistance over longer time intervals, due to easy diffusion paths for oxygen through the pores and boundaries. The ZSA631 shows a significant amount of silica on the surface. Active oxidation of silica above 1700 °C would render such a scale unusable as well. ZSA82 and ZSA721, on the other hand, show a mix of ZrO$_2$ and SiO$_2$. Furthermore, these samples seem to have a denser surface as compared to ZS73.

The mass change and the oxide scale thickness data after the 10-min oxidation are presented in Table 2. ZS73 and ZSA631 lose significant amount of mass, while ZS82 gains mass. Mass change for the ZSA721 sample is minimal. This agrees well with the analytical
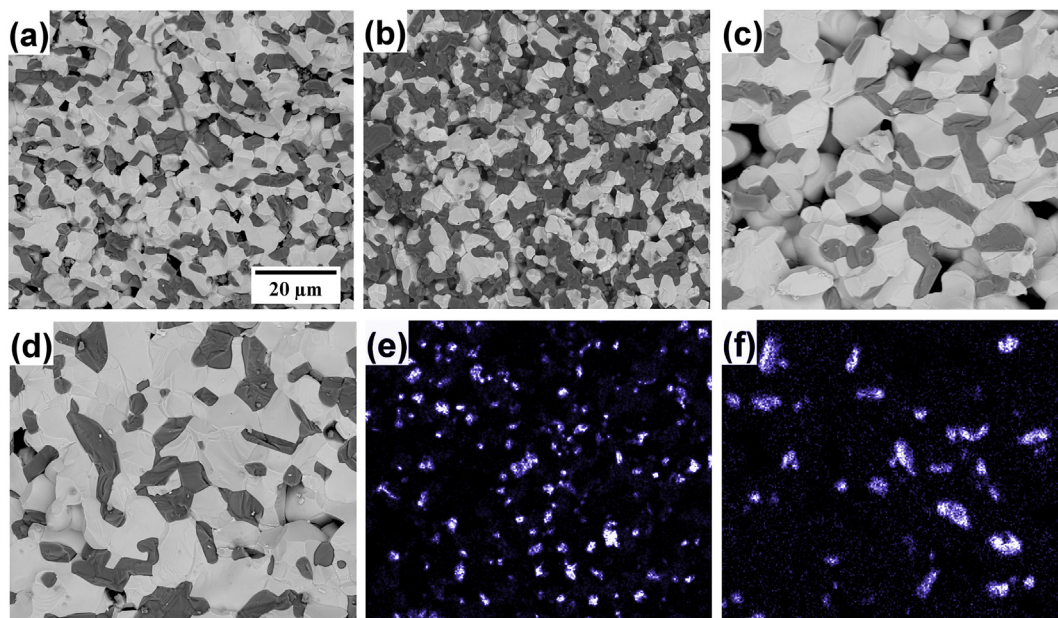
Fig. 2. SEM micrographs of sintered samples: a. ZS73, b. ZSA631, c. ZSA721 d. ZS82; and Al elemental EDS maps: e. ZSA631, f. ZSA721. All six images share the same magnification.
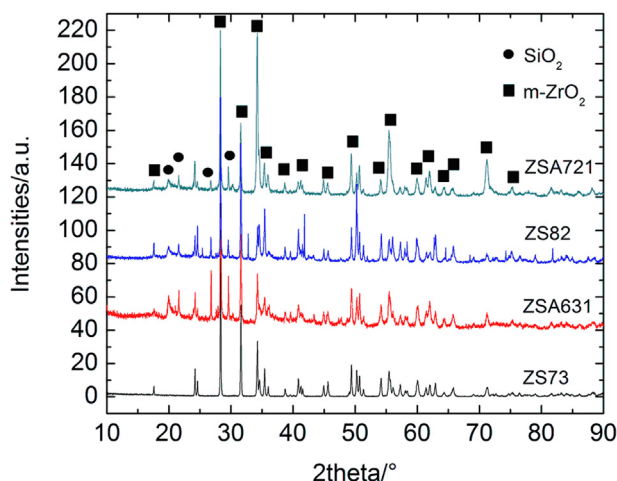

Fig. 3. XRD pattern of samples surfaces after 10 min oxidation in plasma.

prediction from Parthasarathy et al. [16] that evaporation of SiO is significant above 1600 °C, which leads to a large mass loss, as well as a more severe mass loss in samples having a higher SiC content. The sample, ZS73, shows the highest, ZS82 shows the minimum, while ZS631 and ZSA721 are comparable in overall scale thickness. Savino et al. [17] reported scale thickness around 150 μm after 6.4 min of arc jet exposure around 1780 to 1810°C—the same order of magnitude compared to current samples. Given the higher testing temperature and long exposure time as well as higher Si content, it is reasonable the scale thickness of the current samples is higher.

The cross-section SEM and corresponding EDS maps are shown in Fig. 5. These results are consistent with the results provided in Table 2, with the maximum scale thickness observed in the ZS73 sample and the minimum observed in the ZS82 sample. In all samples, the scale primarily consists of ZrO_2. Si completely depletes in ZS73, while still is present in ZSA631, ZS82, and ZSA721. ZSA631 shows the highest Si amount. Elemental distribution of Al is shown

in Fig. 5b (ZSA631) and 4d (ZSA721). The ZSA631 sample shows an Al-rich top layer.

Thermodynamically-stable oxides for the ZrB_2-SiC-AlN system include Al_2O_3, SiO_2, B_2O_3, and ZrO_2. Destabilization of the stable oxides is possible only at extremely low oxygen pressures. For instance, the destabilizing of these oxides at 2027 °C (2300 K) requires an oxygen pressure below 10^{-10} atm. The stability of the oxides also depends on their relevant vapor species. For instance, as shown in Fig. 1b, an increase in the temperature from 1527 to 2027 °C (1800−2300 K) results in more than two orders of magnitude increase in B_2O_3 vapor pressure. At the current test temperature, B_2O_3 is expected to evaporate significantly, once it forms. During the experiment, a green fluorescence was observed at the initial stage of the plasma exposure, but diminished after a few minutes. This green fluorescence emission corresponds to volatilization of the boron species [18]. EDS further confirmed boron is largely absent from the surface. SiO_2 has a sufficiently low vapor pressure that it is not likely to vaporize as gas phase SiO_2. However, SiO_2 is prone to volatilization during active oxidation according to the following reaction [19]:

$$SiO_2 \ (l) \rightarrow SiO \ (g) + 0.5O_2 \ (g) \tag{1}$$

This reaction is accompanied by a decrease in mass. The high vapor pressure of SiO is likely to result in a large depletion of the Si species at high temperatures. The highest vapor pressure in Al species is more than one order of magnitude lower than Si species. Therefore, Al should be less prone to depletion in comparison with Si. At the testing temperature (~2027 °C), the Al_2O_3 vapor pressure is of the order of 10^{-3} atm [20], while the oxygen partial pressure needed for formation of Al_2O is less than $10^{-11.8}$ atm. The oxygen partial pressure at ZrB_2-ZrO_2 interface at 2027 °C, based on Fig. 1a, is $10^{-10.43}$ atm, higher than the oxygen partial pressure of Al_2O. Hence, thermodynamically, Al_2O_3 would form instead of Al_2O (the formation of some Al_2O is possible, due to uncertainties in temperature and other variables). ZrO_2 is unlikely to volatilize from the surface, since its vapor ZrO reaches only $10^{-5.58}$ atm at 2027 °C (2300 K). Therefore, the thermodynamically favorable overall surface oxides would be ZrO_2 and possibly some SiO_2 and Al_2O_3. Not
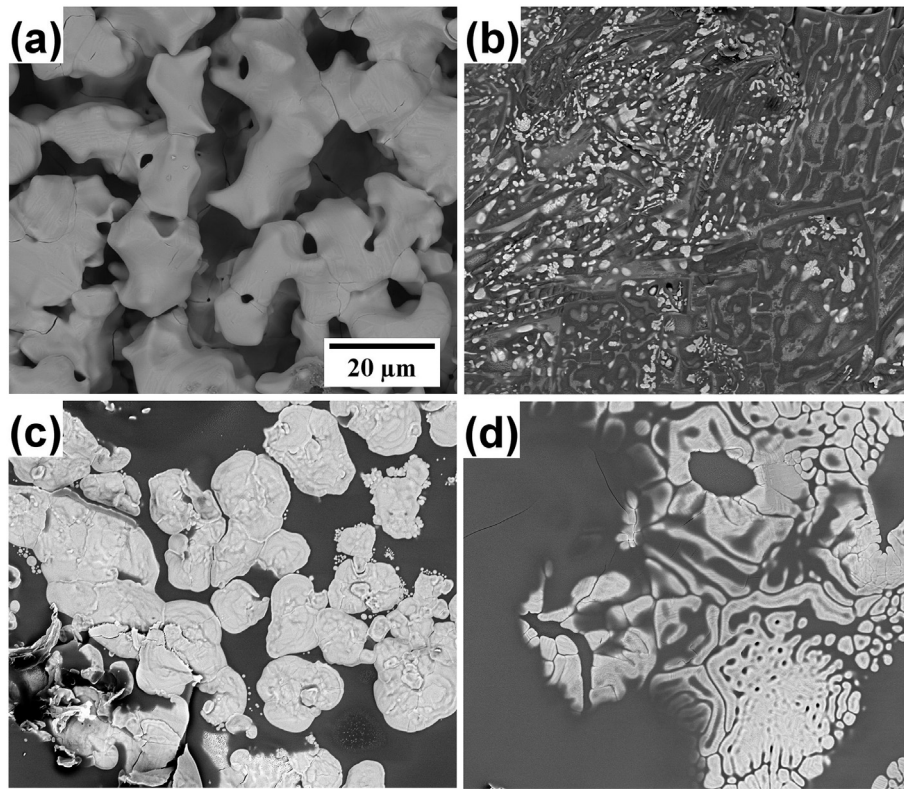
Fig. 4. Surface micrographs of 10-min tests samples. Micrographs a-d shows the representative features of the samples ZS73, ZSA631, ZS82, ZSA721 respectively. All four images share the same magnification.

Table 2
Mass change data and oxygen scale thickness for samples after 10 min tests.

Sample	Mass change (mg/cm^2)	Scale thickness (μm)
ZS73	−11.3	498 ± 42
ZSA631	−10.1	287 ± 55
ZS82	10.7	262 ± 62
ZSA721	−0.1	325 ± 82

surprising, both ZrO_2 and SiO_2 are observed in the XRD pattern and SEM micrographs (except for ZS73, which shows the presence of ZrO_2 only). The absence of SiO_2 in the diffraction pattern of ZS73 is consistent with the surface micrographs of ZS73 (Fig. 4a), which shows a preponderance of ZrO_2 clusters, but no visible SiO_2 glassy outer scale. The EDS map (Fig. 5a) suggests a large oxygen-affected region and indicates the presence of SiO_2 at depths below 300 μm from the surface; hence, no detection by x-rays. On the other hand, ZS82 (Fig. 5c) has a thinner scale. As a result, the SiO_2 is sufficiently close to the surface and observed in the corresponding XRD
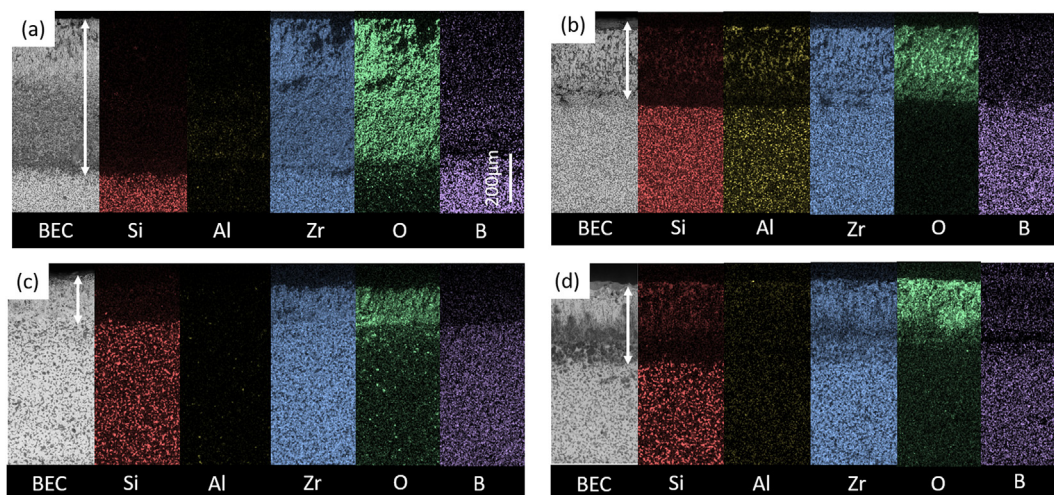

Fig. 5. Cross-section SEM and EDS maps of 10-min tested samples. (a) ZS73, (b) ZSA631, (c) ZS82, (d) ZSA721. The first column on the left shows the back scattered electron images. The elements mapped in EDS maps are indicated below the EDS maps. The arrow shows the depth of oxygen affect region. All four images share the same magnification.

pattern. ZSA631 and ZSA721 (Fig. 5b and d, respectively) show the presence of Si and Al oxides at the surface.

All samples display a net mass loss after cyclic tests. The mass change is accompanied by oxide scale spallation, with the oxide layer spalling completely in ZS82 (Supplemental Information Fig. S3), possibly because of thermal shock and high stresses, due to the subsonic plasma stream. Since the entire oxide scale for ZS82 spalled off after the second cycle, the sample was not subjected to further cycling. Other samples show varying degrees of oxide scale spallation. Nonetheless, none showed a complete spallation of the scale as observed in ZS82. Mass changes reflect the combined effects of spallation and oxidation. Hence, cross-section microstructures, rather than mass measurements, provide a clearer picture of the oxidation process.

The cross-section micrographs at the end of the cyclic oxidation tests are presented in Fig. 6, with all the sections obtained from the surfaces exposed directly to plasma heating. For ZS73, Fig. 6 (a) shows the scale spalls off in some regions, while remaining intact in other regions. More importantly, an interfacial zone is observed in the sub-surface, underneath the regions from where the scale spalled off. A closer look at this microstructure shows the presence of two interfacial regions. Interestingly, the second interfacial region is present underneath the region where the external scale has spalled off. According to our design rationale, the external ZrO_2 acts as a thermal barrier, resulting in an effective temperature drop. Once the temperature is lower than the active oxidation temperature, silica/aluminosilica provides an oxidation resistant layer. Formation of a Si rich protective layer occurs by outward diffusion of Si [5], which results in the development of a Si depleted region. Once the external scale spalls, the thermal barrier effect is lost, and the silica is exposed to temperatures that rise above the active oxidation temperature, which adversely affects the oxidation

resistance. Oxidation occurs rapidly yet again, following the spallation event, until a sufficiently thick external ZrO_2 layer forms yet again. Therefore, the formation of multiple interfacial regions is likely due to the scale spallation occurring due to thermal shocks in different cycles.

The cross-section microstructure for ZSA631 (Fig. 6b) differs significantly from that of ZS73. The outer layers of the scale for ZSA631 are significantly more porous than the other samples. The inset shows a higher magnification image of the interfacial region between the external oxide scale and the base alloy. EDS analyses (Fig. 7a) in this region confirmed the presence of Al-rich aluminosilicate (dark contrast) along with ZrO_2 (bright contrast). ZSA631 shows the maximum mass change (and recession) during testing with the sample progressively ablated. Unlike the ZS73 sample, the external scale for ZSA631 is not comprised exclusively of zirconia with a fair amount of aluminosilicate with high aluminum content present as well. Fig. 6c shows the cross-section of the ZS82 sample after two cycles, where the external ZrO_2 layer is completely missing. The inset shows the side face of the sample (not directly exposed to the plasma stream during testing). Clearly, the scale spalls off from the exposed face and from a small region on the side of the sample. The scale is still present in the regions exposed to relatively lower temperatures and the scale sub-surface shows a degree of similarity with ZS73, albeit the volume fraction of ZrO_2 is considerably higher and the SiO_2 considerably lower in comparison with ZS73. This is possibly due to the higher Zr content of the pristine alloy in ZS82 as opposed to ZS73. Fig. 6d shows the cross-section microstructure of ZSA721. This sample does not show any obvious scale spallation, but the external ZrO_2 region is interspersed with aluminosilicate. Note, the aluminum content in the scale for the ZSA721 sample is much lower than for the ZSA631 sample as shown in Fig. 7a. The inset shows a high magnification
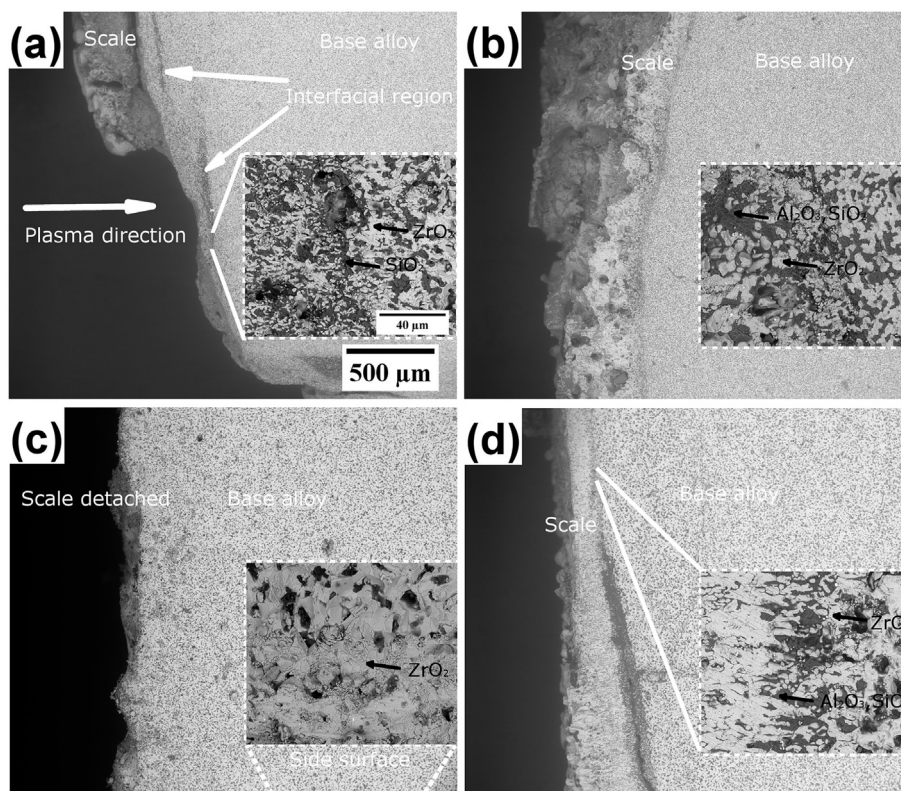

Fig. 6. Cross-section micrographs of samples a. ZS73, b. ZSA631, c. ZS82, d. ZSA721 after cyclic tests (cross-section micrographs pertaining to ZS82 were recorded after two test cycles). All four images share the same magnification.
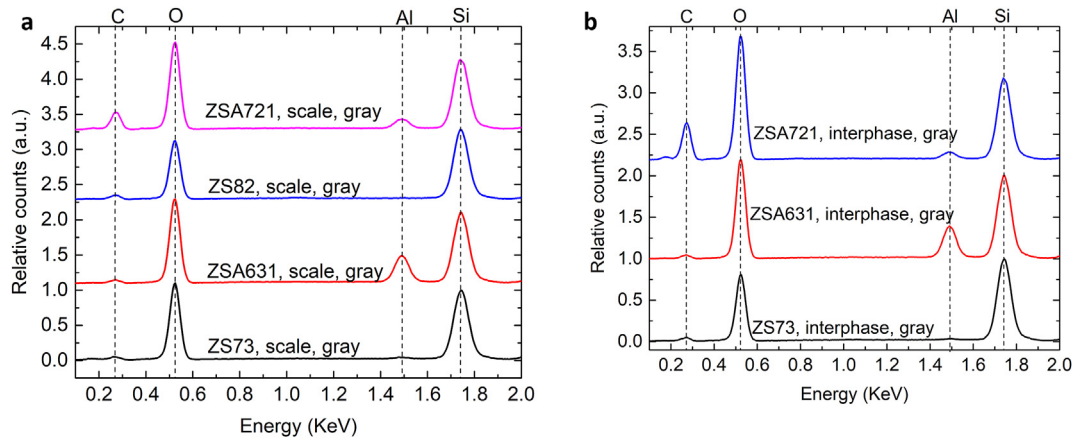
Fig. 7. EDS spectrum of the samples, (a) EDS spectrum of the surface gray region shown in Fig. 5, (b) EDS spectrum of the interphase gray region shown in Fig. 5.

image for the interfacial region between the base alloy and the oxide scale. EDS analyses reveal the interfacial chemistry is a combination of silicon, aluminum, and oxygen, likely consisting of aluminosilicate as shown in Fig. 7b. Again, the aluminum content in this interphase region is lower than for ZSA631.

The presence of an external ZrO_2 layer is likely to modify the temperature profile as a function of depth from the surface. The temperature drop across the external ZrO_2 layer can be approximately estimated using the heat conduction equation:

$$\frac{Q}{t} = \frac{\kappa A (T_1 - T_2)}{d}, \tag{2}$$

where Q is the heat flow, in this case the enthalpy of the plasma jet; t is the time; κ is the thermal conductivity of ZrO_2; T_1, T_2 are the temperature on the sample surface and below ZrO_2; and d is the thickness of the ZrO_2 layer. The heat flux is expected to be close to the range of $250\,W/cm^2$, based on the extrapolated value from the heat fluxes and surface temperatures plotted from the literature [21] using 2000 °C surface temperature. The barrier layer is considered solely ZrO_2. Under these conditions, using the measured thicknesses of ZrO_2 layers from the microstructures, the temperature at the inner face of the ZrO_2 layer can be estimated to be below 1800°C—just below the active oxidation regime for SiC.

Based on these results, we can now elucidate the oxidation mechanism for ZrB_2-SiC-AlN composites at ~2000 °C and 100 Torr pressure. This material oxidizes to form ZrO_2, B_2O_3 (due to the oxidation of ZrB_2), SiO_x, CO_x (due to the oxidation of SiC), Al_2O_3, and NO_x (due to the oxidation of AlN). At the test temperature, 2000 °C, B_2O_3 volatilizes. Similarly, due to active oxidation of SiC, a stable silicate layer does not form. Consequently, the external oxide comprises of ZrO_2, which co-exists with a Si-depleted subscale because of active oxidation. Across the ZrO_2 scale, the temperature eventually drops to 1700 °C or lower. Under these conditions, a stable silicate layer forms, which is modified by the presence of Al_2O_3 in the AlN containing samples. Al_2O_3 modified alloys result in lower viscosity of the silicate, allowing for faster coverage in this region. This layer affords oxidation resistance. As seen in earlier work [9], the Al_2O_3 content is quite critical. If the viscosity reduces drastically (high Al_2O_3 content), this subscale silicate does not afford sufficient tenacity to the overlying ZrO_2. If the viscosity reduction is insignificant (low Al_2O_3 content), the stresses due to the mismatch in the coefficients of thermal expansion $(6.8 \times 10^{-6}\,K^{-1})$ for ZrB_2 [22] and $10.8 \times 10^{-6}\,K^{-1}$ for ZrO_2 [23] of ZrO_2 and the base material cannot be accommodated, thus leading to scale spallation. Similarly, a low viscosity subscale may also fail to

accommodate the transformation stresses arising during the reversible transformation from high temperature tetragonal structure to monoclinic structure in ZrO_2 associated with a volume increase with the volume strain of 4.7% at room temperature [24]. Such a layered structure provides a rationale for designing the UHTC chemistry. The scale structure as shown in Fig. 8 is somewhat analogous to that for a superalloy with a thermal barrier coating. The amount of ZrB_2 should be high enough to form a near exclusive external ZrO_2 scale. The external ZrO_2 acts as the thermal barrier, since ZrO_2 has a relatively low thermal conductivity $(\sim2.2\,Wm^{-1}K^{-1}$ [25]). This thermal barrier protects the underlying material from high temperature damage. The interfacial region between the base alloy and the external scale functions similar to the thermally grown oxide, imparting oxidative stability to the underlying material. Furthermore, columnar zirconia grains are "glued" together, if the interfacial chemistry is appropriate. Pure SiO_2 crystallizes at ultra-high temperatures. If crystalline SiO_2 is present at the base of the columnar ZrO_2, the damage tolerance will be relatively poor. On the other hand, a glassy layer of aluminosilicate with relatively low viscosity will better accommodate the stresses during thermal cycling. Hence, a proper balance of ZrB_2, SiC, and AlN is essential for designing a damage-tolerant, robust UHTC. ZS82 suffered during cyclic tests, due to the presence of excessive ZrO_2, and insufficient strain tolerant glassy interfacial
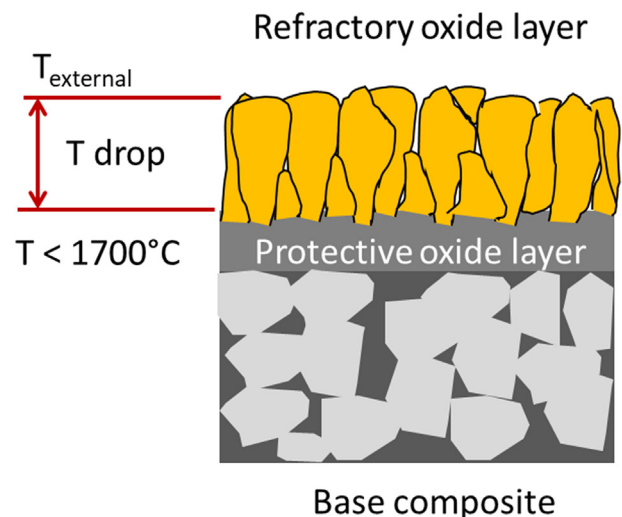

Fig. 8. Schematic of the scale structure after ultra-high temperature oxidation.

layer to accommodate the thermal stresses. To a lesser extent, similar issues occurred with ZS73 (relatively lower ZrO_2 content somewhat mitigated the susceptibility to cyclic damage with respect to ZS82). ZSA631 had a significant aluminosilicate interface, but lacked a near exclusive ZrO_2 scale. In the presence of an adequate "thermal barrier," the oxide scale in ZSA721 performed better under cyclic conditions, since a relatively high ZrB_2 content ensured a ZrO_2-rich external scale, while a high Al:Si ratio with sufficient SiC ensured the presence of an aluminosilicate interlayer anchoring the external columnar ZrO_2 grains.

5. Conclusions

A new design concept involving growth of layered thermal barrier coating and its stabilization for enhanced oxidative stability for ultra high temperature ceramic has been proposed. Such approach mirrors the theme of nickel base super alloy, where the alloy must develop an outer scale with low thermal conductivity and thermal stability to protect the base alloy from high temperature damage, and an interphase with proper viscosity to alleviate the thermal stress of this thermal barrier scale. ZrB_2-SiC-AlN system were found to be of great potential following this design concept, where ZrO_2 grows as the outer thermal barrier layer, and anchored by the aluminum silicate scale whose viscosity can be tuned by varying Al:Si ratio.

Acknowledgements

Appendix A. Supplementary data

Supplementary data to this article can be found online at https://doi.org/10.1016/j.jallcom.2019.03.250.

References

[1] W.C. Tripp, H.H. Davis, H.C. Granham, Effect of an SiC addition on the oxidation of ZrB_2, Am. Ceram. Soc. Bull. 52 (8) (1973) 612–616.

[2] F. Monteverde, A. Bellosi, Oxidation of ZrB_2-based ceramics in dry air, J. Electrochem. Soc. 150 (11) (2003) B552–B559.

[3] W.G. Fahrenholtz, G.E. Hilmas, Oxidation of ultra-high temperature transition metal diboride ceramics, Int. Mater. Rev. 57 (1) (2012) 61–72.

[4] P. Williams, R. Sakidja, J. Perepezko, P. Ritt, Oxidation of ZrB_2-SiC ultra-high temperature composites over a wide range of SiC content, J. Eur. Ceram. Soc. 32 (14) (2012) 3875–3883.

[5] W.G. Fahrenholtz, Thermodynamic analysis of ZrB_2-SiC oxidation: formation of a SiC-depleted region, J. Am. Ceram. Soc. 90 (1) (2007) 143–148.

[6] X.H. Zhang, P. Hu, J.C. Han, Structure evolution of ZrB_2-SiC during the oxidation in air, J. Mater. Res. 23 (7) (2008) 1961–1972.

[7] S.N. Karlsdottir, J.W. Halloran, Rapid oxidation characterization of ultra-high temperature ceramics, J. Am. Ceram. Soc. 90 (10) (2007) 3233–3238.

[8] G. Ouyang, P.K. Ray, M.J. Kramer, M. Akinc, High-temperature oxidation of ZrB_2-SiC-AlN composites at 1600°C, J. Am. Ceram. Soc. 99 (3) (2016) 808–813.

[9] G. Ouyang, P.K. Ray, M.J. Kramer, M. Akinc, Effect of AlN substitutions on the oxidation behavior of ZrB2-SiC composites at 1600°C, J. Am. Ceram. Soc. 99 (10) (2016) 3389–3397.

[10] S.C. Zhang, G.E. Hilmas, W.G. Fahrenholtz, Pressureless sintering of ZrB_2-SiC ceramics, J. Am. Ceram. Soc. 91 (1) (2008) 26–32.

[11] ASTM Standard B962 - 15 Standard Test Methods for Density of Compacted or Sintered Powder Metallurgy (PM) Products Using Archimedes' Principle, West Conshohocken, PA, 2015.

[12] M.W. Chase, NIST-JANAF Thermochemical Tables, fourth ed., American Institute of Physics, Washington, DC, New York, 1998.

[13] M.M. Opeka, I.G. Talmy, J.A. Zaykoski, Oxidation-based materials selection for 2000 °C + hypersonic aerosurfaces: theoretical considerations and historical experience, J. Mater. Sci. 39 (19) (2004) 5887–5904.

[14] T. Karahan, G. Ouyang, P.K. Ray, M.J. Kramer, Mufit Akinc, Oxidation mechanism of W substituted Mo-Si-B alloys, Intermetallics 87 (2017) 38–44.

[15] X.H. Zhang, P. Hu, J.C. Han, S.H. Meng, Ablation behavior of ZrB_2-SiC ultra high temperature ceramics under simulated atmospheric re-entry conditions, Compos. Sci. Technol. 68 (7–8) (2008) 1718–1726.

[16] T.A. Parthasarathy, R.A. Rapp, M. Opeka, M.K. Cinibulk, Modeling oxidation kinetics of SiC-containing refractory diborides, J. Am. Ceram. Soc. 95 (1) (2012) 338–349.

[17] R. Savino, M.D. Fumo, D. Paterna, A. Di Maso, F. Monteverde, Arc-jet testing of ultra-high-temperature-ceramics, Aero. Sci. Technol. 14 (3) (2010) 178–187.

[18] M. Playez, D.G. Fletcher, J. Marschall, W.G. Fahrenholtz, G.E. Hilmas, S.M. Zhu, Optical emission spectroscopy during plasmatron testing of ZrB_2-SiC ultrahigh-temperature ceramic composites, J. Thermophys. Heat Transf. 23 (2) (2009) 279–285.

[19] A. Rezaie, W.G. Fahrenholtz, G.E. Hilmas, Oxidation of zirconium diboride-silicon carbide at 1500 °C at a low partial pressure of oxygen, J. Am. Ceram. Soc. 89 (10) (2006) 3240–3245.

[20] W.M. Haynes, CRC Handbook of Chemistry and Physics, CRC press, 2014.

[21] T.H. Squire, J. Marschall, Material property requirements for analysis and design of UHTC components in hypersonic applications, J. Eur. Ceram. Soc. 30 (11) (2010) 2239–2251.

[22] N.L. Okamoto, M. Kusakari, K. Tanaka, H. Inui, M. Yamaguchi, S. Otani, Temperature dependence of thermal expansion and elastic constants of single crystals of ZrB_2 and the suitability of ZrB_2 as a substrate for GaN film, J. Appl. Phys. 93 (1) (2003) 88–93.

[23] T.I.A. Kosolapova, Handbook of High Temperature Compounds : Properties, Production, Applications, Hemisphere Pub. Corp., New York, 1990.

[24] M. Ruhle, A.G. Evans, High toughness ceramics and ceramic composites, Prog. Mater. Sci. 33 (2) (1989) 85–167.

[25] G.V. Samsonov, The Oxide Handbook, second ed., Wiley-VCH Verlag GmbH & Co. KGaA, New York and London, 1982.